Composites Part B 201 (2020) 108373

Contents lists available at ScienceDirect

Composites Part B

journal homepage: www.elsevier.com/locate/composites

A continuum constitutive model for FDM 3D printed thermoplastics

S. Garzon-Hernandez [a,b,*], A. Arias [a], D. Garcia-Gonzalez [a,**]

[a] Department of Continuum Mechanics and Structural Analysis, University Carlos III of Madrid, Avda. de la Universidad 30, 28911 Leganés, Madrid, Spain
[b] Current affiliation: Department of Engineering Science, University of Oxford, Parks Road, Oxford OX1 3PJ, UK

ARTICLE INFO

Keywords:
Additive manufacturing
Fused deposition modelling (FDM)
3D printed polymer
Mechanical behaviour
Constitutive model

ABSTRACT

Fused deposition modelling (FDM) is the most common additive manufacturing technology used for thermoplastic components. This layers-based manufacturing process results into direct links between printing parameters and the polymer mesostructure by means of porosity and structural anisotropy. These dependencies along with other features of thermoplastic polymers (i.e., nonlinearities, viscous and thermal responses) makes its constitutive modelling very challenging. This work distances from studies that model the 3D printing process. Instead, we aim at complementing such approaches with a continuum model to describe the macroscopic behaviour of FDM thermoplastics while preserving links with printing parameters. Prior to the modelling conceptualisation, experimental characterisation tests are conducted on ABS specimens to evaluate the influence of printing parameters on the macroscopic mechanical response. The physical fundamentals behind the deformation and failure mechanisms are identified and motivate the new constitutive model. This model is formulated for finite deformations within a thermodynamically consistent framework. The model accounts for: nonlinear response; anisotropic hyperelasticity related to a transversely isotropic distribution of porous; strain rate dependency; macroscopic stiffness dependent on 3D printing processing. Finally, the model is numerically implemented and calibrated for ABS with original experiments, demonstrating its suitability.

1. Introduction

Additive manufacturing or three-dimensional (3D) printing technologies has led to an industrial revolution, allowing the manufacturing of components by the addition of material layers from a CAD file. This comes down to the integration of the design and manufacturing processes, efficient use of the material with minimal waste and great opportunities for customised geometries [1]. Despite all these advantages, 3D printing techniques still offer inferior mechanical properties due to additional porosity and anisotropy caused by the nature of the manufacturing process by layers [2]. In this regard, both porosity and mechanical anisotropy strongly depend on the printing parameters. Therefore, far from considering these as disadvantages, the influence of printing parameters may be used to customise the mechanical properties of the printed components by imposing intricate porosity patterns.

Among all 3D printing techniques, fused deposition modelling (FDM) is the most common for thermoplastics and reinforced thermoplastic materials such as acrylonitrile butadiene styrene (ABS), polylactic acid (PLA) [2], polycarbonate [3], Ultem [4], polyether-ether-ketone (PEEK) [5] or fibre reinforced thermoplastics [6,7]. FDM offers a great versatility to fabricate thermoplastic components with complex 3D geometry in reasonable manufacturing times, thus becoming a good alternative for applications in different sectors such as the aeronautical, automotive, and biomedical industries [2,8]. However, despite the advances in this field, there is still limited knowledge about the links between the manufacturing process conditions and the final mechanical performance of these components, impeding further progress and exploitation of this technology.

Prior to deepen into FDM polymers, a proper understanding of traditional thermoplastics is needed. These polymers reach large deformations presenting nonlinear response, pressure, temperature and strain rate dependencies. Some of these dependences have also been observed in FDM materials by other authors, e.g. increase in elastic modulus and yield strength with strain rate [9–11]. Moreover, the mechanical properties of FDM components are sensitive to printing parameters that affect the mesostructure [12]. Some printing parameters have already been analysed experimentally in the literature: the influence of layer thickness [12–14]; air gap [12,15]; printing temperature [5,14–16]; or feed rate [17]. In this regard, a decrease in layer thickness or an increase in printing temperature result in a

* Corresponding author at: Department of Continuum Mechanics and Structural Analysis, University Carlos III of Madrid, Avda. de la Universidad 30, 28911 Leganés, Madrid, Spain.
** Corresponding author.
E-mail addresses: sgarzon@ing.uc3m.es (S. Garzon-Hernandez), danigarc@ing.uc3m.es (D. Garcia-Gonzalez).

https://doi.org/10.1016/j.compositesb.2020.108373
Received 21 May 2020; Received in revised form 12 August 2020; Accepted 17 August 2020
Available online 27 August 2020

decrease of void density, thus leading to higher elastic modulus and yield stress [13,14,16]. Furthermore, filaments are deposited with a preferential alignment causing a marked anisotropic behaviour [9,13,15,18–20]. The results from these works show that specimens manufactured with a 0° (longitudinal) raster orientation present the highest tensile performance; while specimens with a 90° (transversal) raster angle present the weakest. Therefore, further optimisation of FDM components and their applications requires the identification of manufacturing process dependences on the deformation mechanisms of these materials. To this end, the development of reliable constitutive models can help to guide their design and optimisation. Current efforts to date approach the 3D printing manufacturing process describing the interplay between thermo-mechanical processes providing direct links between printing parameters and the final mesostructure [21]. The current work distances from these approaches and aims to complement them by providing a continuum model describing the macroscopic behaviour of FDM thermoplastics while still linking it to printing parameters. However, such modelling is very challenging as all the aforementioned considerations must be taken into account together.

The macroscopic mechanical response of traditional thermoplastic materials has extensively been modelled in the current literature. Among these approaches, one of the first advanced models to predict their mechanical response is the hyperelastic–viscoplastic model proposed by Arruda and Boyce [22]. This model captures strain rate and temperature dependences as well as strain softening in glassy polymers. Mulliken and Boyce [23] proposed a model which captures the transition in the yield behaviour and large strain post-yielding over a wide range of temperatures and strain rates. More recently, Polanco-Loria and co-authors developed a constitutive model to predict the response of thermoplastic materials under isothermal conditions [24,25]. Nguyen et al. [26] proposed a phenomenological constitutive model to capture the pressure- and rate-dependent mechanical response of amorphous glassy polymers including a softening variable to capture strong nonlinearities. More recently, Garcia-Gonzalez and co-authors have studied the mechanical behaviour of semi-crystalline polymers and have proposed a series of models to reproduce the mechanical behaviour of semi-crystalline polymers accounting for viscous effects and thermo-mechanical coupling [27–29]. Another alternative is the application of time-fractional models for the computation of viscous responses [30], which can be also applied for damage evolution [31]. Regarding the constitutive modelling of 3D printed polymers, most of the models to date are formulated for infinitesimal deformations and based on linear elasticity combined with a yield criterion for orthotropic materials [3,20,32,33]. Zou et al. [20] provided a comparison between two modelling approaches: isotropic linear elasticity and transversely isotropic linear elasticity. However, these models are insufficient to predict the inelastic deformation process of 3D printed polymers under large deformations and do not include links with the printing process.

Despite the efforts made to date to model the mechanical behaviour of 3D printed polymers, to the authors' knowledge, there is no constitutive model available in the literature accounting for the principal characteristics of both elastic and inelastic responses of such type of materials. In this paper, a hyperelastic constitutive model is proposed to describe the mechanical behaviour of FDM thermoplastics. We distance from modelling the thermo-mechanics of the 3D printing manufacturing process, and focus on the final links between printing parameters and the effective macroscopic behaviour of FDM thermoplastics. This model is developed for finite deformations within a thermodynamically consistent framework and accounts for: nonlinear response; anisotropic hyperelasticity related to a transversely isotropic distribution of porous; strain rate dependency; macroscopic stiffness dependent on 3D printing processing. Some of the previous dependencies can be directly linked to the 3D printing parameters used during the manufacturing process. To motivate the principal bases and assumptions of the model, an experimental characterisation campaign is conducted on FDM ABS specimens.

Table 1
Printing parameters.

Printing parameter	Value
Infill density	100%
Road width	0.4 mm
Air gap	0 mm
Infill pattern	Lines
Printing temperature	240 °C
Build plate temperature	100 °C

Table 2
Void density as a function of layer height.

Layer height (mm)	Mean void density (%)
0.1	1.1
0.2	2.28
0.3	4.45

These results are shown in Section 2 analysing the influence of some printing parameters and strain rate, permitting the identification of the physical fundamentals behind the deformation and failure mechanisms that govern the mechanical behaviour of FDM thermoplastics. Section 3 presents the formulation of the constitutive model proposed in this work. Section 4 describes the numerical implementation and the identification of the model parameters for FDM ABS. The corresponding results and discussion are presented in Section 5. Finally, Section 6 concludes this work.

2. Experimental characterisation of FDM thermoplastics

The aim of this section is to identify the physical fundamentals behind the mechanical behaviour of FDM printed materials and to establish the basis of the constitutive model proposed. To this end, we provide a detailed characterisation of FDM ABS to analyse the influence of two printing parameters: layer height and raster orientation; and strain rate in terms of stress–strain response and failure mechanisms. In addition, the influence of the number of layers and the corresponding interfaces formed is approached.

2.1. Material and methods

To study the macroscopic mechanical response of ABS FDM components, experimental tensile tests are conducted at two different strain rates ($3 \cdot 10^{-4}$ s^{-1} and $3 \cdot 10^{-3}$ s^{-1}). Thin rectangular specimens with dimensions 164 mm × 50 mm are printed in ABS. This geometry has been chosen to avoid premature failure due to stress concentration in the radius of the fillet observed in 3D printed dog-bone geometry samples [13,34].

The influence of 3D printing parameters has been studied considering three different layer heights (0.1, 0.2 and 0.3 mm), two rasters orientations (longitudinal and transverse) and different number of layers (from one to three), giving a total number of eighteen different specimen-type groups. All the specimens are manufactured with unidirectional layers to have a better control on the effects of the parameters studied. The remaining parameters are hold at the recommended or default values, see Table 1. Moreover, only a single contour is deposited along the component edge in all the specimens, to avoid the influence of the contours on the mechanical properties [35]. A total number of four specimens per condition are tested to obtain reliable results.

2.2. Experimental results

2.2.1. Mechanical dependencies and stress–strain response

The layer height has a great influence on the final mesostructure and, therefore, on the porosity of FDM components. To study this influence, the cross-sectional area of the specimens was previously

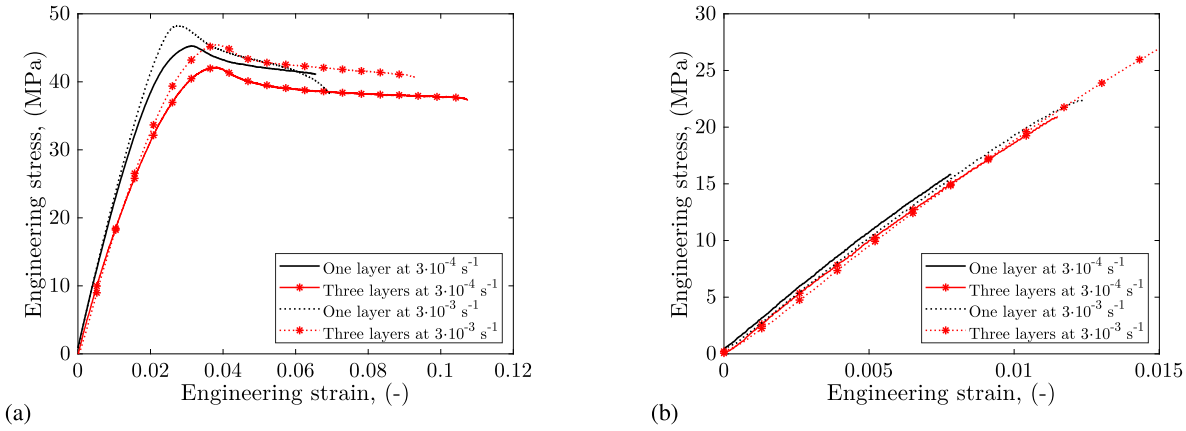

Fig. 1. Comparison of stress–strain response of 0.1 mm FDM ABS specimens at different strain rates: (a) longitudinal and (b) transversal orientations.

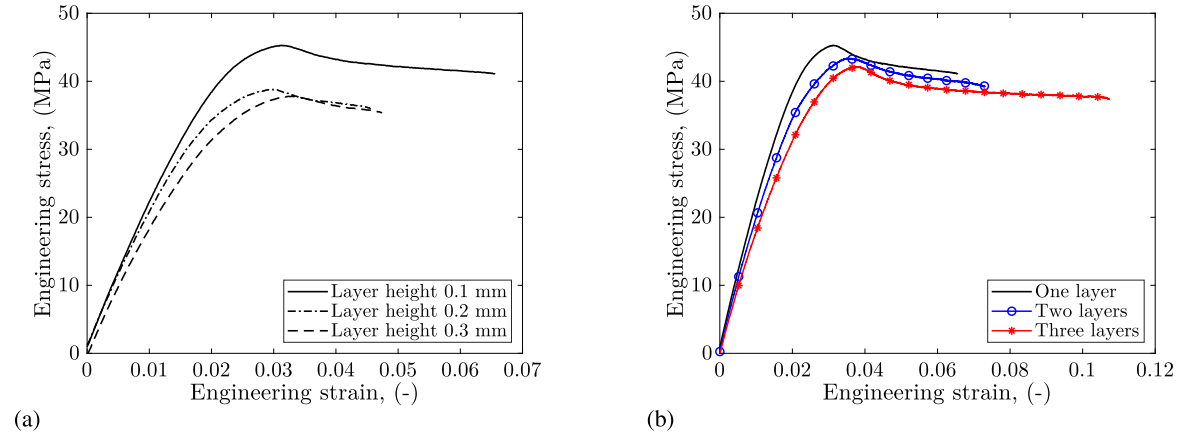

Fig. 2. Comparison of stress–strain response of longitudinal FDM ABS specimens at a strain rate of $3 \cdot 10^{-4}$ s^{-1}: (a) one layer and three different layer heights and (b) 0.1 mm layer height and three different number of layers.

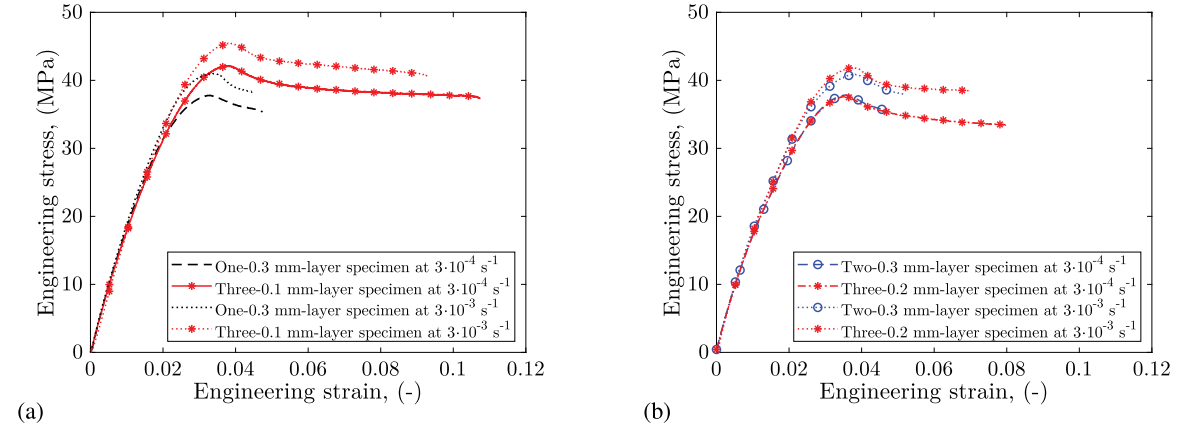

Fig. 3. Comparison of stress–strain response of longitudinal FDM ABS specimens with the same total thickness at different strain rates: (a) total thickness of 0.3 mm and (b) total thickness of 0.6 mm.

analysed with a scanning electron microscope and estimated by image techniques. The average results are summarised in Table 2, where an increase in porosity is observed when layer height increases.

The effect of the strain rate on the mechanical response of FDM thermoplastics is shown in Fig. 1, where the stress–strain response of specimens with a layer height of 0.1 mm is presented for both raster orientations. A slight increase is observed in the Young's modulus as strain rate increases for both longitudinal and transverse. Moreover, a more noticeable increase in the yield stress is observed for longitudinal specimens, and in the ultimate tensile strength for transversal ones. On the other hand, comparing the mechanical response for both raster orientations, higher Young's modulus and maximum stress is observed for longitudinal specimens. Note that maximum stress corresponds to yield stress for longitudinal specimens and ultimate tensile strength for transversal specimens. These tendencies are in accordance with the previous studies found in the literature [9–11].

The dependences with the layer height and number of layers are shown in Fig. 2. Higher performance, in terms of Young's modulus

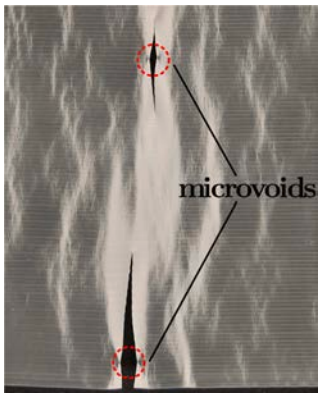

Fig. 4. Shear bands and crazing on a longitudinal one-0.1 mm-layer specimen tested at a strain rate of $3 \cdot 10^{-4}$ s^{-1}.

and maximum stress, is observed as layer height decreases, being the effect more significant when the layer height decreases from 0.2 mm to 0.1 mm than from 0.3 mm to 0.2 mm, see Fig. 2a. These tendencies are explained by the previous results shown in Table 2, where an increase in void density is observed with layer height. In the same way, a lower mechanical response, in terms of Young's modulus and maximum stress, is observed when the number of layers increases, see Fig. 2b. These differences in mechanical response are explained by the fact that when the number of layers increases so does the number of bonding interfaces. In this regard, a steady limit is expected for a given number of layers, from which the mechanical response would not be altered. The definition of such limit needs of further studies and is out of the scope of this work.

Finally, Fig. 3 compares the response of specimens with the same thickness (i.e., one-0.3 mm-layer specimens vs. three-0.1 mm-layers specimens or two-0.3 mm-layers specimens vs. three-0.2 mm-layers specimens). Better performance is obtained with a smaller layer height due to lower porosity. However, similar mechanical properties are obtained for the case of specimens with a total thickness of 0.6 mm and a longitudinal raster orientation, as shown in Fig. 3b.

More details of these experimental results are shown in Appendix.

2.2.2. Deformation and failure mechanics

As for mechanical properties such as Young's modulus and maximum stress, the deformation mechanisms and failure modes observed during deformation and fracture also depend on the printing parameters, especially on the raster orientations. Longitudinal specimens present a linear elastic region followed by necking and, finally, a plastic flow at constant stress. During the deformation process of longitudinal specimens, shear zones appeared on each filament and propagate obliquely before yielding. In addition, crazes formation and growth are observed. Crazing develops when excessive stress is applied to the polymer, leading to microvoid formation normal to the loading direction [36], see Fig. 4. These crazing and shear banding continue propagating along the whole gauge length. From the microvoids, cracks start to propagate slowly at first but rapidly when the cross section is reduced. Finally, the fracture occurs normal to the loading direction leading to stress whitened areas, see Fig. 4. The fracture surface is also analysed with an optical microscope, where micro-shearing is observed on each filament, see Figs. 5a and 5b.

On the other hand, transverse specimens exhibit a linear elastic behaviour with a brittle fracture. The fracture occurs along the filament-to-filament interface as observed when comparing Figs. 5c and 5d. This is explained by the fact that, in transverse specimens, the loads are taken by the bond between filaments and not by the filaments themselves.

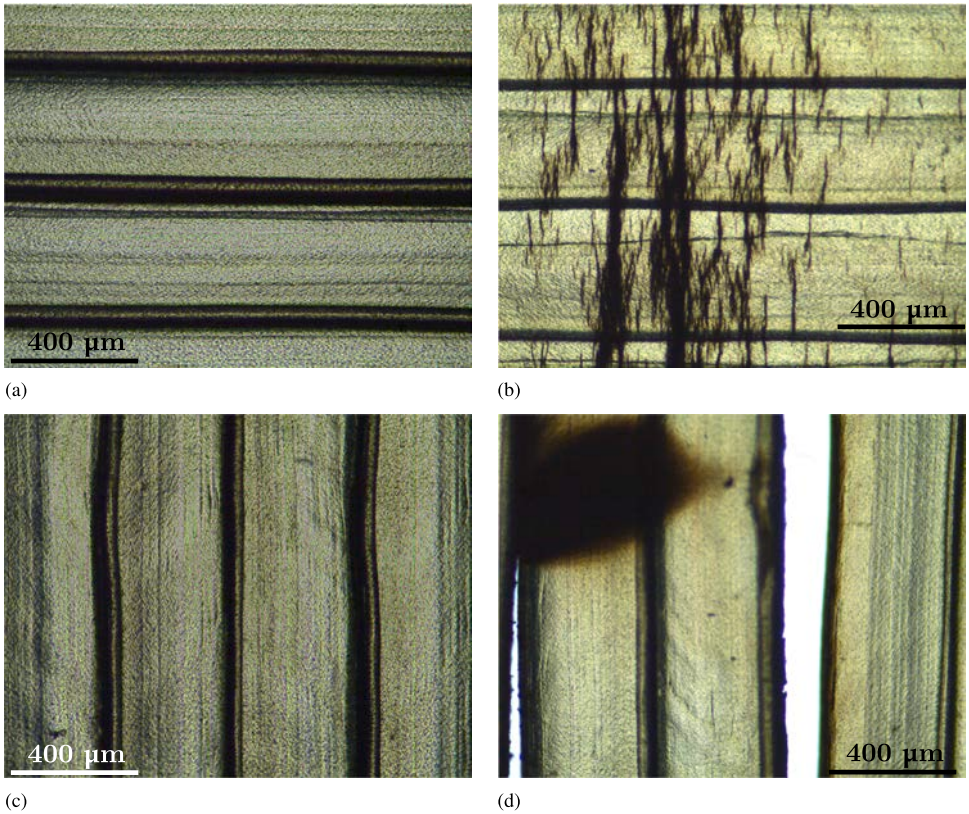

Fig. 5. Microphotograph of superficial surface of a one-0.1 mm-layer specimen tested at a strain rate of $3 \cdot 10^{-4}$ s^{-1}: (a) longitudinal before testing and (b) after testing; (c) transversal before testing and (d) after testing.

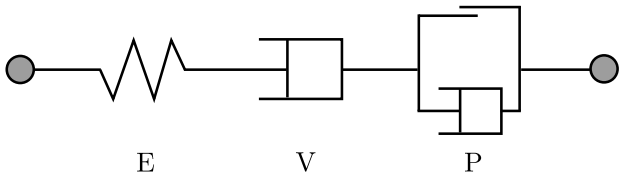

Fig. 6. Rheological scheme of the proposed constitutive.

3. Constitutive model

In the previous section, the layer height has been identified as a key parameter influencing the final mesostructure. This parameter has a great influence on the porosity (void density) of the final structure, strongly influencing the mechanical performance. Moreover, the mechanical anisotropy of FDM components has been found to strongly depend on the orientation of filaments deposition and porosity distribution. In addition, the number of layers affects the mechanical performance of these components due to the density of bonding interfaces. On the other hand, the nature of thermoplastic polymers is complex so viscoelastic and viscoplastic behaviours play a relevant role in the overall mechanical response.

In this paper, a hyperelastic constitutive model is developed to describe the macroscopic mechanical behaviour of FDM thermoplastics. This model is developed for finite deformations within a thermodynamically consistent framework and accounts for: nonlinear response; anisotropic hyperelasticity related to a transversely isotropic distribution of porous; strain rate dependency; macroscopic stiffness dependent on 3D printing processing. Some of the previous dependencies can be directly linked to the 3D printing parameters used during the manufacturing process. In this regard, the dependency of the mechanical response with the layer height is introduced by the void density (porosity). Moreover, a softening model is used to include the influence of the number of layers. This section presents the proposed continuum mechanics model including the description of the rheological scheme, the finite deformation kinematics and the thermodynamics.

To help the understanding of the model formulation, the list of symbols used is provided in Table 3.

3.1. Rheological model

From experimental results, it is observed that FDM polymers present an viscoelastic–viscoplastic anisotropic behaviour. Therefore, the rheological model is composed of a purely elastic anisotropic spring (E) followed by two dashpots, see Fig. 6. The former (V) accounts for viscoelastic dependencies while the second one (P), which is in parallel with a friction element, accounts for viscoplasticity. The friction element represents a yield function controlling the plastic flow activation. Note that the viscoelastic response is intimately described associating the elastic spring and the first viscous dashpot. Therefore, we define these two rheological elements in front of the viscoplastic dashpot acting on top.

According to the rheological model, the total stress is equal on the three components

$$\boldsymbol{\sigma} = \boldsymbol{\sigma}_{\boldsymbol{E}} = \boldsymbol{\sigma}_{\boldsymbol{V}} = \boldsymbol{\sigma}_{\boldsymbol{P}} \tag{1}$$

3.2. Kinematics

The finite deformation kinematics is defined by four configurations going from an initial reference configuration Ω_0 to a current configuration Ω, see Fig. 7. Two additional intermediate configurations have been added. The former refers to as a dilated configuration $\bar{\Omega}$ in which only viscoplastic deformation is accounted for, while the second one refers to as a dilated relaxed configuration $\bar{\bar{\Omega}}$ in which both viscoelastic and viscoplastic deformations are considered. Therefore, the total deformation gradient can be multiplicatively decomposed as

$$\boldsymbol{F} = \boldsymbol{F}_{\boldsymbol{E}}\boldsymbol{F}_{\boldsymbol{V}}\boldsymbol{F}_{\boldsymbol{P}} \tag{2}$$

where $\boldsymbol{F}_{\boldsymbol{E}}$ is the elastic component and $\boldsymbol{F}_{\boldsymbol{V}}$ and $\boldsymbol{F}_{\boldsymbol{P}}$ are the viscoelastic and viscoplastic components, respectively.

Table 3
Nomenclature used for the constitutive formulation.

$\Omega_0, \bar{\Omega}, \bar{\bar{\Omega}}, \Omega$	Initial, dilated, dilated relaxed and current configurations
$\boldsymbol{\Psi}$	Helmholtz free-energy function
e_0	Specific internal energy per unit volume in Ω_0
η_0	Specific entropy per unit volume in Ω_0
θ_0	Reference temperature
$\boldsymbol{Q}$	Heat flux per unit volume in Ω_0
R	Heat source per unit volume in Ω_0
$\boldsymbol{a}_0$	FDM filament orientation
$\boldsymbol{I}$	Second-order identity tensor
$\boldsymbol{F}$	Deformation gradient
$\boldsymbol{F}_{\boldsymbol{E}}, \boldsymbol{F}_{\boldsymbol{V}}, \boldsymbol{F}_{\boldsymbol{P}}$	Elastic, viscoelastic and viscoplastic deformation gradients
$\boldsymbol{J}$	Jacobian
$\boldsymbol{C}$	Right Cauchy–Green strain tensor
$\boldsymbol{B}$	Left Cauchy–Green strain deformation
I_i	Principal invariants of **C**
$\boldsymbol{\sigma}$	Cauchy stress tensor
$\boldsymbol{\sigma}_{\mathbf{E}}, \boldsymbol{\sigma}_{\mathbf{V}}, \boldsymbol{\sigma}_{\mathbf{P}}$	Elastic, viscoelastic and viscoplastic Cauchy stress tensor
$\boldsymbol{P}$	First Piola–Kirchhoff stress tensor
$\boldsymbol{l}$	Velocity gradient in Ω
$\boldsymbol{l}_{\boldsymbol{E}}$	Elastic velocity gradient in Ω
$\bar{\mathbf{L}}_{\mathbf{V}}$	Viscoelastic velocity gradient in $\bar{\Omega}$
$\bar{\bar{\mathbf{L}}}_{\mathbf{P}}$	Viscoplastic velocity gradient in $\bar{\bar{\Omega}}$
$\boldsymbol{N}_{\boldsymbol{p}}$	Direction tensor of the plastic flow
ζ	Softening variable
μ_m	Matrix shear modulus
v_m, v_f	Initial matrix and voids volume fractions
n	Shear modulus porosity-sensitivity parameter
ζ_∞	Dimensionless maximum softening
α	Phenomenological softening parameter
ι	Softening saturation parameter
η	Viscosity
q_1, q_2	Material parameters of the yield function
σ_{kk}	Transverse hydrostatic stress
σ_{eqv}	Equivalent von Mises stress
σ_y	Yield stress
σ_s	Saturation stress
H	Hardening/softening parameter
$\bar{\varepsilon}_p$	Equivalent plastic strain
$\dot{\gamma}_p$	Viscoplastic multiplier
$\dot{\varepsilon}_0$	Reference strain rate
C	Rate-sensitivity parameter

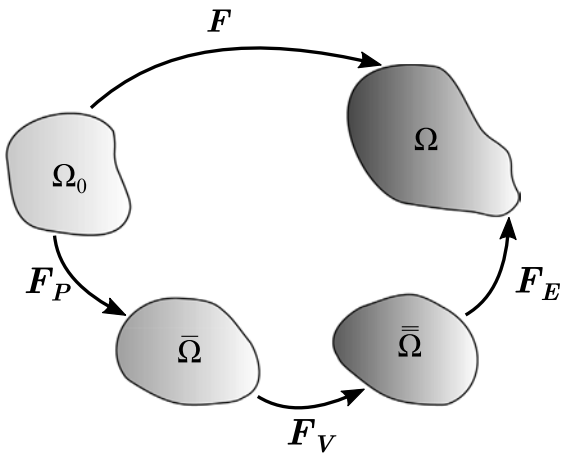

Fig. 7. Kinematics of the proposed constitutive.

The velocity gradient $\boldsymbol{l}$ can be written, according to the kinematics of the model, as

$$\boldsymbol{l} = \boldsymbol{l}_{\boldsymbol{E}} + \boldsymbol{F}_{\boldsymbol{E}}\bar{\bar{\boldsymbol{L}}}_{\boldsymbol{V}}\boldsymbol{F}_{\boldsymbol{E}}^{-1} + \boldsymbol{F}_{\boldsymbol{E}}\boldsymbol{F}_{\boldsymbol{V}}\bar{\boldsymbol{L}}_{\boldsymbol{P}}\boldsymbol{F}_{\boldsymbol{V}}^{-1}\boldsymbol{F}_{\boldsymbol{E}}^{-1} \tag{3}$$

where $\boldsymbol{l}_{\boldsymbol{E}} = \dot{\boldsymbol{F}}_{\boldsymbol{E}}\boldsymbol{F}_{\boldsymbol{E}}^{-1}$ is the elastic component of the velocity gradient in Ω, $\bar{\bar{\boldsymbol{L}}}_{\boldsymbol{V}} = \dot{\boldsymbol{F}}_{\boldsymbol{V}}\boldsymbol{F}_{\boldsymbol{V}}^{-1}$ is the viscoelastic component defined in $\bar{\bar{\Omega}}$ and $\bar{\boldsymbol{L}}_{\boldsymbol{P}} = \dot{\boldsymbol{F}}_{\boldsymbol{P}}\boldsymbol{F}_{\boldsymbol{P}}^{-1}$ is the viscoplastic component defined in $\bar{\Omega}$. Both viscoelastic and viscoplastic velocity gradients are equal to the symmetric parts of the corresponding velocity gradients since the configurations $\bar{\Omega}$ and $\bar{\bar{\Omega}}$ are assumed to be invariant to the rigid body rotations of Ω.

3.3. Thermodynamics

The constitutive relations of the model have to satisfy the first and second laws of thermodynamics to ensure thermodynamic consistency, which are expressed per unit of reference volume as

$$\dot{e}_0 = \boldsymbol{P} : \dot{\boldsymbol{F}} - Div\boldsymbol{Q} + R \tag{4a}$$

$$\dot{\eta}_0 \geq -Div\left(\frac{\boldsymbol{Q}}{\theta_0}\right) + \frac{\mathrm{R}}{\theta_0} \tag{4b}$$

The constitutive modelling of a hyperelastic material is constructed from the definition of a Helmholtz free-energy function Ψ per unit of reference volume, that can be defined as a function of the specific internal energy and entropy per unit reference volume by

$$\Psi = \mathrm{e}_0 - \theta_0\eta_0 \tag{5}$$

and expressed in its rate form

$$\dot{\mathrm{e}}_0 = \dot{\Psi} + \dot{\theta}_0\eta_0 + \theta_0\dot{\eta}_0 \tag{6}$$

The choice of the energy function is motivated on the deformation mechanisms and material dependences observed from the experiments performed. In this regard, to account for viscous effects, Ψ is assumed to depend on $\boldsymbol{F}$, $\boldsymbol{F}_V$ and $\boldsymbol{F}_P$. Furthermore, to introduce transverse isotropy of 3D printed polymers, the strain energy function also depends on the preferred direction of the material $\boldsymbol{a}_0$ and, therefore, can be introduced as $\Psi = \Psi(\boldsymbol{F}, \boldsymbol{F}_V, \boldsymbol{F}_P, \boldsymbol{a}_0)$. Moreover, there is a strong influence of the number of layers leading to lower stiffness and mechanical performance. This dependence is included in the energy function by a softening model as

$$\Psi = (1-\zeta)\Psi_0(\boldsymbol{F}, \boldsymbol{F}_V, \boldsymbol{F}_P, \boldsymbol{a}_0) \tag{7}$$

where ζ is the softening parameter which depends on the number of layers. In addition, the experimental results show important dependences of the mechanical behaviour of FDM polymers on printing parameters such as layer height. All these experimental observations are taken into account in the definition of the energy function, which is further particularised in detail in Section 3.4.

The rate form of Ψ can be derived using the chain rule as

$$\dot{\Psi} = (1-\zeta)\left[\frac{\partial\Psi_0}{\partial\boldsymbol{F}} : \dot{\boldsymbol{F}} + \frac{\partial\Psi_0}{\partial\boldsymbol{F}_{\boldsymbol{V}}} : \dot{\boldsymbol{F}}_{\boldsymbol{V}} + \frac{\partial\Psi_0}{\partial\boldsymbol{F}_{\boldsymbol{P}}} : \dot{\boldsymbol{F}}_{\boldsymbol{P}}\right] \tag{8}$$

Note that ζ depends on the manufacturing process and remains constant during the deformation process. Combining both laws with Eqs. (6) and (8), the Clausis–Duhem inequality is rewritten as

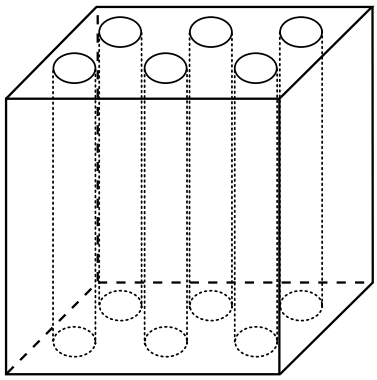

Fig. 8. Matrix with aligned continuous cylindrical pores isotropically distributed.

$$\left(\boldsymbol{P} - (1-\zeta)\frac{\partial\Psi_0}{\partial\boldsymbol{F}}\right) : \dot{\boldsymbol{F}} - \left(\frac{\partial\Psi}{\partial\theta_0} + \eta_0\right)\dot{\theta}_0 - (1-\zeta)\frac{\partial\Psi_0}{\partial\boldsymbol{F}_{\boldsymbol{V}}} : \dot{\boldsymbol{F}}_{\boldsymbol{V}} - (1-\zeta)\frac{\partial\Psi_0}{\partial\boldsymbol{F}_{\boldsymbol{P}}} : \dot{\boldsymbol{F}}_{\boldsymbol{P}} - \frac{\boldsymbol{Q}Grad\theta_0}{\theta_0} \geq 0 \tag{9}$$

This inequality must be satisfied for all thermo-mechanical processes. The terms $\frac{\partial\Psi_0}{\partial\boldsymbol{F}_{\boldsymbol{V}}} : \dot{\boldsymbol{F}}_{\boldsymbol{V}}$ and $\frac{\partial\Psi_0}{\partial\boldsymbol{F}_{\boldsymbol{P}}} : \dot{\boldsymbol{F}}_{\boldsymbol{P}}$ are related to viscous dissipation and $\boldsymbol{Q}Grad\theta_0$ corresponds to the thermal conduction (neglected in this work as isothermal conditions are assumed). Therefore, applying Coleman–Noll arguments [37,38], the first Piola–Kirchhoff stress tensor $\boldsymbol{P}$ and entropy can be derived as

$$\boldsymbol{P} = (1-\zeta)\frac{\partial\Psi_0}{\partial\boldsymbol{F}} \tag{10a}$$

$$\eta_0 = -\frac{\partial\Psi}{\partial\theta_0} \tag{10b}$$

Eq. (10a) relates a stress tensor with the strain energy function and a deformation-related tensor. This relation can be arbitrarily expressed by means of the Cauchy stress tensors $\boldsymbol{\sigma}$ as

$$\boldsymbol{\sigma} = (1-\zeta)\frac{2}{\boldsymbol{J}}\boldsymbol{F}\frac{\partial\Psi_0}{\partial\boldsymbol{C}}\boldsymbol{F}^{\boldsymbol{T}} \tag{11}$$

where $\boldsymbol{C} = \boldsymbol{F}^{\boldsymbol{T}}\boldsymbol{F}$ is the total right Cauchy–Green deformation tensor.

3.4. Constitutive equations

3.4.1. Visco-hyperelastic resistance

FDM is an extrusion process where components are built layer by layer by the union of melt filaments. The mesostructure of the resulting components leads to orthotropic materials composed by polymeric filaments partially bonded and voids [39]. In this regard, they can be approached as a matrix reinforced by continuous aligned voids as shown in Fig. 8. Note that a circular cross-section of the void fibres is considered as a first approach.

Thus, the elastic resistance is defined by the strain energy function developed for neo-Hookean composites with aligned continuous cylindrical pores by [40]

$$\begin{aligned}\Psi_0(\boldsymbol{C}_{\boldsymbol{E}}, \boldsymbol{a}_0) = \Psi_0(I_1^E, I_3^E, I_4^E) &= \frac{\mu_m\upsilon_m}{2}\left(I_4^E + 2I_4^{E^{-1/2}} - 3\right) \\ &+ \frac{\mu_m}{2}(J-1)I_4^{E^{-1/2}}\ln\left(\frac{J-\upsilon_m}{J\upsilon_f}\right) \\ &+ \frac{\mu_m\upsilon_m}{2(1+\upsilon_f)}\left(I_1^E - I_4^E - 2\sqrt{\frac{I_3^E}{I_4^E}}\right)\end{aligned} \tag{12}$$

where υ_m and υ_f are the initial volume fractions of the matrix and the voids ($\upsilon_m + \upsilon_f = 1$), respectively, μ_m is the shear modulus of the matrix, $I_1^E = trace(\boldsymbol{C}_{\boldsymbol{E}})$, $I_3^E = det(\boldsymbol{C}_{\boldsymbol{E}})$ and $I_4^E = \boldsymbol{a}_0\boldsymbol{C}_{\boldsymbol{E}}\boldsymbol{a}_0$. Note that the energy function from Eq. (7) is alternatively defined by means of $\boldsymbol{a}_0$ and the elastic right Cauchy–Green deformation tensor $\boldsymbol{C}_{\boldsymbol{E}} =$

$\boldsymbol{F}_E^T \boldsymbol{F}_E$. This energy is based on an additive decomposition of the total free energy into: an isochoric uniaxial deformation along the preferred direction, an equi-biaxial deformation on the transverse plane, and a subsequent shear deformation. The Cauchy stress tensor can be derived from Eqs. (11) and (12).

The parameter μ_m is the shear modulus of the material itself and, from the experimental results, it is proven that the mechanical properties for specimens with different layer heights are different. This differences in stiffness cannot be captured alone with effective elastic properties accounting for the porosities as done by other authors [41]. An extra dependence arises from differences in the molecular organisation of the chains during the printing process due to the amount of material extruded in each condition. This difference in μ_m must be considered on top of the pure effect of porosity and is defined, as a first approach and based on experimental tendencies, by an exponential function as

$$\mu_m = \mu_{m0}(1 - v_f)^n \tag{13}$$

where μ_{m0} is the shear modulus of the bulk material and n is a material parameter introducing an extra dependency on porosity [42].

Finally, the softening variable, which describes the dependency with the number of layers, is given by

$$\zeta = \zeta_\infty[1 - exp(-\alpha/\imath)] \tag{14}$$

where ζ_∞ describes the dimensionless maximum softening (i.e the maximum softening of the printed polymer with respect to the bulk material that is observed because of increasing the number of layers) and $\alpha = (Z - 1)$, with Z being the number of layers. In addition, $\imath$ is referred to as the softening saturation parameter, that is the number of layers Z from which the softening does not increase.

For the definition of the viscoelastic component of the velocity gradient in Ω, the expression used by Garcia-Gonzalez [43] and Garcia-Gonzalez and Landis [44] is taken

$$\boldsymbol{L_v} = \frac{1}{\sqrt{2}\eta}\boldsymbol{\sigma} \tag{15}$$

where η is the viscosity, which is assumed constant for all the cases.

3.4.2. Viscoplastic resistance

In the rheological model, the viscoplastic dashpot is defined in parallel to a friction element. This friction element governs the activation of the plastic flow by a yield function dependent on void fraction of 3D printed materials. Note that the materials used for FDM are glassy or semi-crystalline polymers and, therefore, the plastic yielding mainly occurs by shear deformation mechanisms (e.g. shear transformation zones [45,46]). As this work focuses on thin layers of FDM printed polymers subjected to tensile conditions, although the hydrostatic stress usually has a relevant influence on the yielding, we avoid to include such dependency on the yielding of the bulk material here. In addition, the experimental results, see Figs. 4 and 5, show shear bands suggesting the dominance of shear mechanisms during the plastic deformation. The modelling of shear yielding in porous materials has been previously addressed in the literature by Gurson based criteria, even for polymeric materials showing a good predictive capability [47,48]. Therefore, we propose the use of a Gurson type model for long cylindrical voids (previously). To this end, the yield function proposed by Gurson [49] and modified by Tvergaard [50,51] is chosen as

$$f = \frac{{\sigma_{eqv}}^2}{{\sigma_0}^2} + 2v_f q_1 \cosh\left(q_2 \frac{\sqrt{3}}{2}\frac{\sigma_{kk}}{\sigma_0}\right) - (1 + (q_1 v_f)^2) = 0 \tag{16}$$

where q_1 and q_2 are material parameters that control the dependency with the porosity, σ_{kk} is the transverse hydrostatic stress to filament (or porous) direction, i.e. $\sigma_{kk} = \sigma_{22} + \sigma_{33}$ if $\boldsymbol{a}_0 = [100]$, σ_{eqv} is the equivalent von Mises stress and σ_0 follows an isotropic softening Voce law as

$$\sigma_0 = (1 - \zeta)\left(\sigma_y + (\sigma_s - \sigma_y)\left[1 - \exp(-H\bar{\varepsilon}_p)\right]\right) \tag{17}$$

where σ_y is the yield stress, σ_s is the saturation stress, H is the softening parameter and $\bar{\varepsilon}_p$ is the equivalent plastic strain. Since the yield stress is influenced by the number of layers, Eq. (17) also includes a softening variable.

The viscoplastic part of the velocity gradient in Ω is defined by an associated viscoplastic flow rule as

$$\boldsymbol{L_P} = \dot{\gamma}_p \boldsymbol{N_p} \tag{18}$$

where $\dot{\gamma}_p$ is a viscoplastic multiplier providing the magnitude of the plastic flow and $\boldsymbol{N_p}$ is a tensor that provides its direction. This last tensor is obtained by deriving the yield function with respect to the Cauchy stress as

$$\boldsymbol{N_p} = \frac{\partial f}{\partial \boldsymbol{\sigma}} \tag{19}$$

Finally, the rate of flow is taken to follow a thermally activated process of Arrhenius type [52] that can be rewritten [24] as

$$\dot{\gamma}_p = \begin{cases} 0 & \text{if f}\leq 0 \\ \dot{\varepsilon}_0 \left[\exp\left[\frac{1}{C}\left(\frac{\sigma_{eqv}}{\sigma_T} - 1\right)\right] - 1\right] & \text{if f} > 0 \end{cases} \tag{20}$$

where $\dot{\varepsilon}_0$ and C are rate-sensitivity parameters and σ_T derives from Eq. (16) as

$$\sigma_T = \left[{\sigma_0}^2(1 + (q_1 v_f)^2) - 2{\sigma_0}^2 v_f q_1 \cosh\left(q_2 \frac{\sqrt{3}}{2}\frac{\sigma_{kk}}{\sigma_0}\right)\right]^{1/2} \tag{21}$$

4. Numerical implementation and model calibration

This section introduces the numerical implementation of the proposed model. In addition, the correspondence of the model parameters with the mechanical response of FDM thermoplastics and their identification for FDM ABS is presented.

4.1. Numerical implementation of the model

The model previously described is numerically implemented to reproduce the uniaxial tensile stress–strain response. Apart from the numerical implementation of the constitutive equations, this numerical cases requires the additional implementation of a Newton–Raphson integration algorithm to calculate the progressive compressible deformation of the structure during the application of the load. To this end, the following residual is defined as

$$\boldsymbol{R}_{long} = \begin{bmatrix}\sigma_{22} \\ \sigma_{33}\end{bmatrix} = 0 \tag{22a}$$

$$\boldsymbol{R}_{trans} = \begin{bmatrix}\sigma_{11} \\ \sigma_{33}\end{bmatrix} = 0 \tag{22b}$$

where Eq. (22a) represents the cases when the load is applied longitudinally to the filaments direction (X direction) and Eq. (22b) represents the cases when the load is applied transversally to the filaments direction (Y or Z direction). σ_{11}, σ_{22} and σ_{33} are the Cauchy stress components in the X, Y and Z directions, respectively. The stiffness or iteration matrix, can be expressed by means of the stretch components as:

$$\boldsymbol{K}_{long} = \begin{bmatrix}\frac{\partial\sigma_{22}}{\partial\lambda_2} & \frac{\partial\sigma_{22}}{\partial\lambda_3} \\ \frac{\partial\sigma_{33}}{\partial\lambda_2} & \frac{\partial\sigma_{33}}{\partial\lambda_3}\end{bmatrix} \tag{23a}$$

$$\boldsymbol{K}_{long} = \begin{bmatrix}\frac{\partial\sigma_{11}}{\partial\lambda_1} & \frac{\partial\sigma_{11}}{\partial\lambda_3} \\ \frac{\partial\sigma_{33}}{\partial\lambda_1} & \frac{\partial\sigma_{33}}{\partial\lambda_3}\end{bmatrix} \tag{23b}$$

The final numerical scheme is shown in Fig. 9.

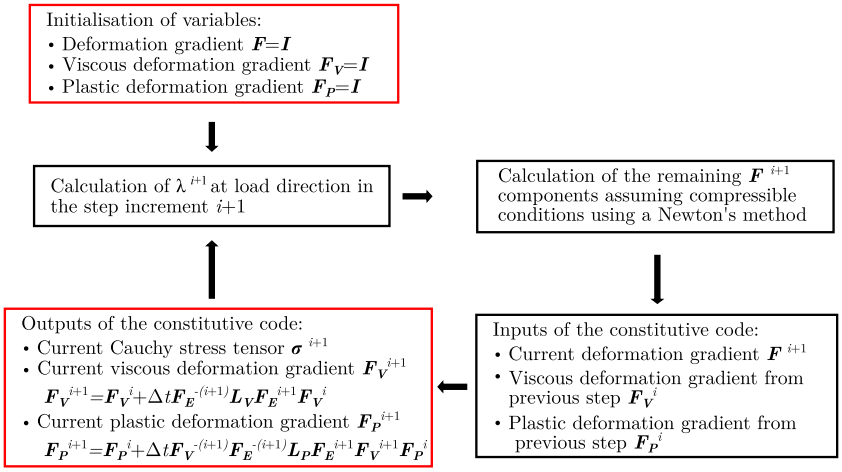

Fig. 9. Numerical implementation scheme.

4.2. Identification of model parameters for FDM ABS

Here, the identification of the parameters of the previously proposed constitutive model is presented for FDM ABS. The void density value used for each layer height is shown in Table 2.

Taking as reference the result obtained for longitudinal one-0.1 mm-layer components at a strain rate of $3 \cdot 10^{-4}$ s^{-1} and considering $\boldsymbol{a}_0 = \begin{bmatrix}1 & 0 & 0\end{bmatrix}$, the model parameters are identified based on their correspondence with the mechanical response following four blocks:

1. *Visco-hyperelastic response*
   The model parameters μ_{m0} and n determine the hyperelastic response of the material. Moreover, the parameter η governs the linear viscoelastic response and is calibrated against experimental results at different strain rates.
2. *Yield stress*
   The parameters σ_y, σ_s and H define the yielding process, while q_1 and q_2 are parameters to capture the dependency of the yield stress with void density. Because of plasticity is only reached when the load is applied along the filaments direction ($\sigma_{kk}=0$), the value of q_2 is not identified in this work.
3. *Viscoplastic response*
   $\dot{\varepsilon}_0$ and C are associated with the nonlinear viscoplastic dashpot. The former is set at the lower strain rate used for the experimental tests, while the second one controls the strain rate dependency on yielding.
4. *Softening model*
   Although the elastic response is modelled as a porous hyperelastic function, the experimental results have shown that the stiffness and strength of specimens manufactured by FDM are not only a function of the void density but also of the number of layers. Therefore, an overall softening of the material associated to the 3D printed process is included to reproduce the dependency of the shear modulus and yield stress with the number of layers. The maximum softening value ζ_∞ is set constant for all the cases. However, the rate with which this value is reached is different for shear modulus (ι_μ) and yield stress (ι_{σ_0}), and for longitudinal (L) and transverse (T) components.

Some parameters can be directly identified by their physical meaning, i.e., the shear modulus of the bulk material (μ_{m0}). In addition, other material parameters are directly identifiable from the experiments by means of mechanical response tendencies: i.e., the material parameter (n), the yield stress (σ_y), the saturation stress (σ_s), the softening parameter (H). Finally, all the phenomenological parameters have been calibrated following the same optimisation procedure used in [53], which consists of a sequential quadratic programming method (*fmincon*, in MATLAB terminology). The parameters for FDM ABS material are provided in Table 4.

Table 4
Material parameters for FDM ABS.

Elastic response		Viscoelastic response	Softening model			
μ_{m0} (MPa)	n	η (MPa s)	ζ_∞	ι_{μ_L}	ι_{μ_T}	ι_{σ_0}
780	4.7	$4.5 \cdot 10^5$	0.7	7	14	30
Viscoplastic response						
σ_y (MPa)	σ_s (MPa)	H	q_1	q_2	$\dot{\varepsilon}_0$ (s^{-1})	C
34.4	31.9	110	4.2	–	$3 \cdot 10^{-4}$	0.028

5. Results and discussion

This section analyses the suitability of the model to predict the mechanical behaviour of FDM polymers for different printing and loading conditions. To this end, model predictions are compared with the original experiments to analyse the predictive capability on:

1. FDM ABS specimens manufactured with different layer heights (0.1, 0.2 and 0.3 mm).
2. FDM ABS specimens manufactured with different raster orientation (longitudinal and transverse).
3. FDM ABS specimens manufactured with different number of layers (from one to three).
4. FDM ABS specimens tested at different strain rates ($3 \cdot 10^{-4}$ s^{-1} and $3 \cdot 10^{-3}$ s^{-1}).
5. FDM ABS specimens tested at load–unload uniaxial tension at a strain rate of $3 \cdot 10^{-4}$ s^{-1}.

The ability of the model to predict the elastic nonlinear and yielding behaviours of FDM ABS depending on different void densities is presented in Fig. 10. This figure compares model predictions and experimental data for one layer specimens with three different layer heights at $3 \cdot 10^{-4}$ s^{-1}. The model is able to capture the anisotropic response and the dependence on porosity. Good agreement between the model predictions and experimental data is found in terms of elastic slope and yielding. However, although the yield function used in this work captures the dependence on porosity for layer heights of 0.1 and 0.3 mm, a higher error is observed for 0.2 mm specimens. This is due to the particular behaviour of these 0.2 mm specimens where their maximum stress is similar to the one obtained for 0.3 mm specimens. Note that the modelled response with respect to this printing parameter (layer height) is not directly defined but it is accounted for by means of

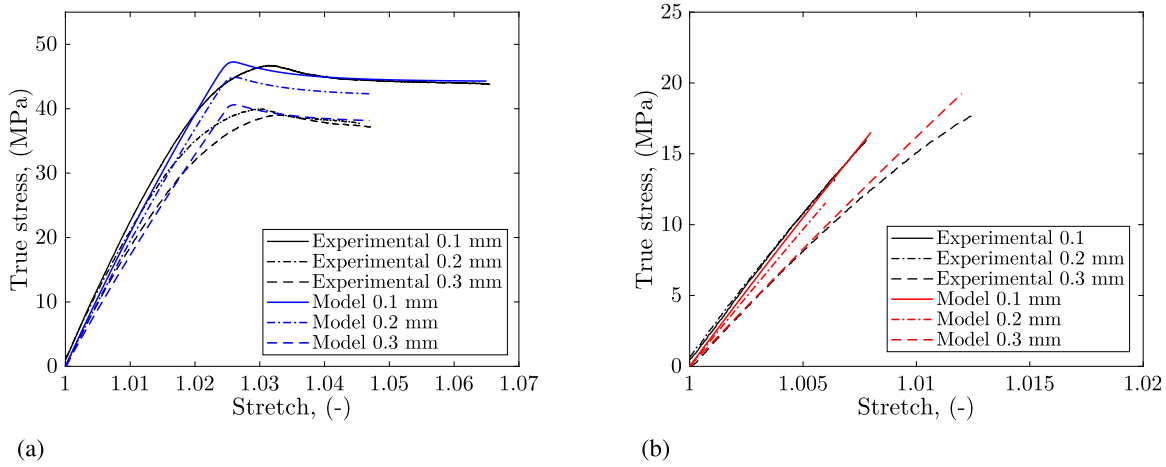

Fig. 10. Comparison of experimental stress–strain response versus model predictions of one layer FDM ABS specimens with three different layer heights at a strain rate of $3{\cdot}10^{-4}$ s^{-1}: (a) longitudinal and (b) transversal.

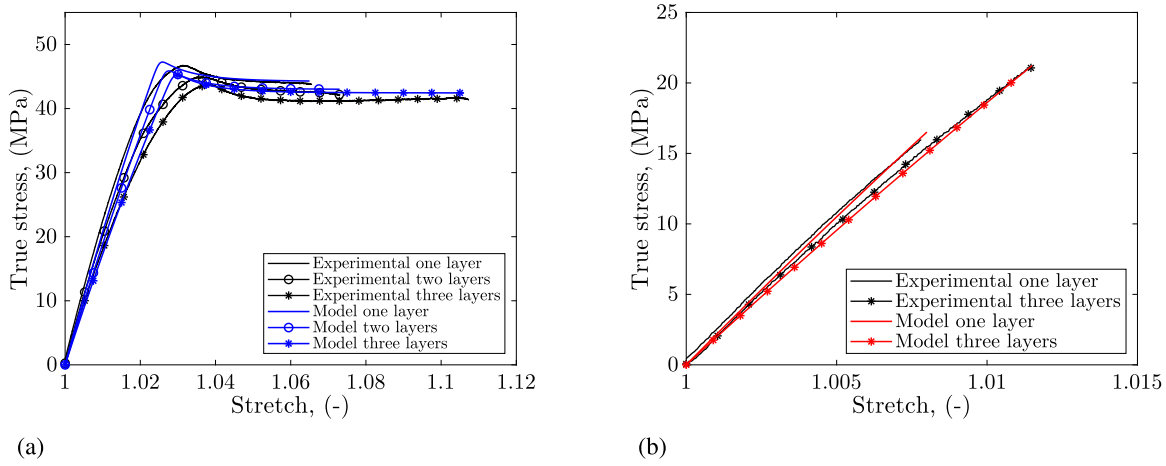

Fig. 11. Comparison of experimental stress–strain response versus model predictions of 0.1 mm layer height FDM ABS specimens at a strain rate of $3 \cdot 10^{-4}$ s^{-1}: (a) longitudinal specimens with different number of layers and (b) transversal specimens with different number of layers.

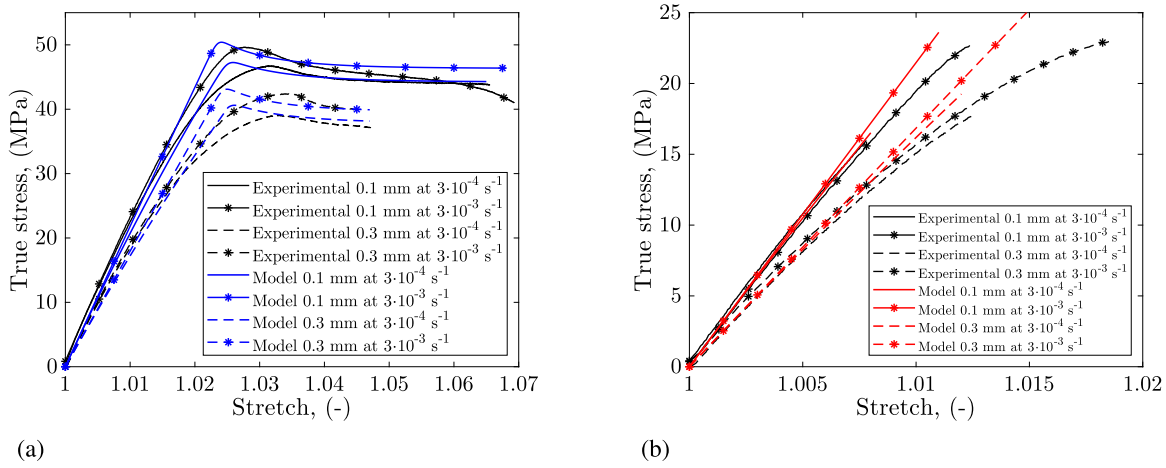

Fig. 12. Comparison of experimental stress–strain response versus model predictions of one layer FDM ABS specimens at different strain rates: (a) longitudinal 0.1 and 0.3 mm layer height specimens and (b) transversal 0.1 and 0.3 mm layer height specimens.

the resulting porosity. In this regard, we captured these dependencies by the Gurson model without including any extra term, for the sake of simplicity as a first approach.

On the other hand, experimental results show that the mechanical response of FDM thermoplastics is influenced by the number of layers due to manufacturing imperfections and interfaces between filaments.

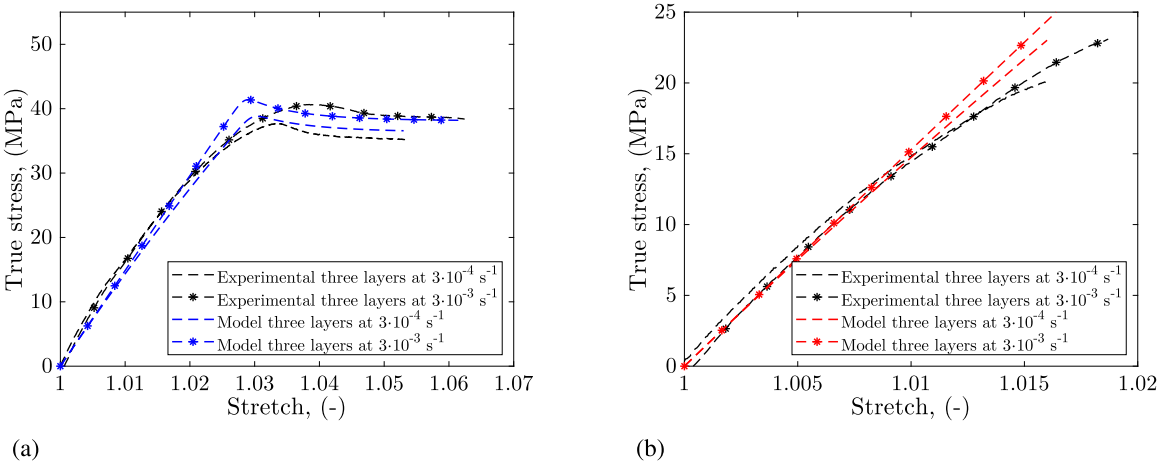

Fig. 13. Comparison of experimental stress–strain response versus model predictions of three-0.3 mm-layer FDM ABS specimens at different strain rates: (a) longitudinal specimens and (b) transversal specimens.

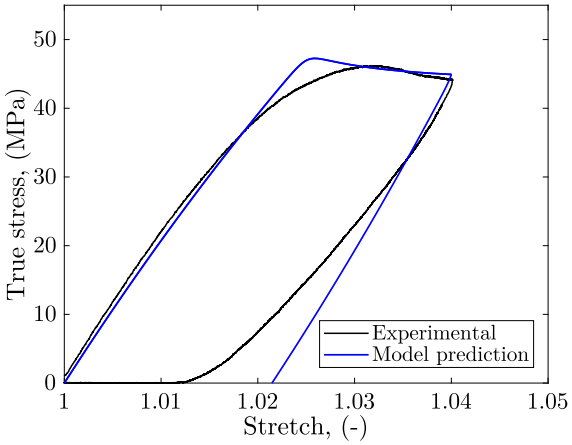

Fig. 14. Comparison of experimental load–unload tensile response versus model predictions of one-0.1 mm-layer longitudinal FDM ABS specimens at a strain rate of $3 \cdot 10^{-4}$ s^{-1}.

This particular dependence is included in the model through a softening variable. Experimental data are compared with model predictions for 0.1 mm layer specimens with different number of material layers for both loading directions in Fig. 11. The predictions demonstrate that the proposed model faithfully captures both shear modulus and yield stress dependencies with the number of layers as well as the influence with the raster orientation. However, more experimental tests are needed to fully analyse this dependence and provide the number of layers which constitutes the upper softening limit.

The ability of the model to account for strain rate dependency in both viscoelastic and viscoplastic behaviours is shown in Fig. 12. The results confirm the ability of the proposed model to predict the hardening increase, in both elastic and inelastic parts, with increasing loading rate.

Moreover, with the aim of illustrating the ability of the model to account for both the number of layers and strain rate, Fig. 13 shows the model predictions for three-0.3 mm-layer specimens. Although the dependency with the number of layers is calibrated for 0.1 mm components, a good agreement can be also observed between model and experimental results for specimens with different layer height and for both raster orientations.

Finally, Fig. 14 shows the prediction capability of the model to capture the load–unload tensile response for a one-0.1 mm-layer longitudinal specimen.

In view of the numerical results, it can be concluded that the proposed model constitutes the first continuum approach for finite deformations that accounts for both material and printing dependencies with a proved capability to describe the mechanical behaviour of FDM 3D printed thermoplastic polymers. The model is able to capture with good agreement the dependencies with the layer height, number of layers and loading conditions (direction and strain rate). However, further efforts are needed to complete the constitutive description. In this regard, the model is not able to capture the nonlinear behaviour before yielding and fails at predicting adequately the response of 0.2 mm layer specimens.

6. Conclusions

In this paper, the influence of three printing parameters and strain rate on the mechanical response of FDM 3D printed ABS specimens is experimentally studied: layer height, number of layers and raster orientation. The results show highest performance when the layer height decreases, as a consequence of porosity decrease, and when the filaments are deposited along longitudinal direction. Moreover, the mechanical properties are lower when the number of layers increases, as a consequence of an increase in bonding interfaces between filaments.

Motivated on these original experimental observations, a new constitutive model for FDM 3D printed components is developed for finite deformations within a thermodynamically consistent framework, and accounts for: nonlinear behaviour, strain rate (in both elastic and inelastic responses), transverse isotropy (in both elastic and inelastic responses), porosity and number of layers dependencies. This continuum constitutive framework is formulated in general bases allowing for further improvements. This constitutive framework is particularised and calibrated for FDM 3D printed ABS polymers. A good agreement between numerical predictions and experiments is found in terms of stress–strain curves depending on loading direction, layer height (equivalent to void density here), number of layers and strain rate. The numerical predictions demonstrate the capacity of the proposed model to predict the mechanical behaviour of FDM polymers by a continuum approach. To the authors' knowledge, this model constitutes a novel continuum approach for finite deformations that accounts for both material and printing dependencies with a proved capability to model the mechanical behaviour of FDM 3D printed thermoplastic polymers. Note that this work does not focus on the printing process itself but

Table A.1
Mechanical properties of specimens with a longitudinal and transverse raster orientations at a strain rate of $3 \cdot 10^{-4} s^{-1}$.

Specimen		Longitudinal				Transverse			
Number of layers	Layer	Elastic modulus (MPa)		Maximum stress (MPa)		Elastic modulus (MPa)		Maximum stress (MPa)	
	Height (mm)	Mean	SD	Mean	SD	Mean	SD	Mean	SD
1	0.1	2229.1	41.4	45.3	0.8	2104.9	54.1	18.6	1.6
	0.2	2088.1	26.6	38.9	0.2	1965.6	18.4	15.7	2.3
	0.3	1966.5	39.4	38.1	0.3	1629.2	35.0	18.5	0.8
2	0.1	2056.5	85.3	43.6	0.3	1984.7	59.9	20.2	2.7
	0.2	1874.5	17.1	38.8	0.3	1765.5	64.3	17.9	0.2
	0.3	1821.3	22.9	38.0	0.7	1554.5	45.2	19.6	1.9
3	0.1	1866.0	51.7	42.2	0.1	1974.0	30.3	23.2	3.9
	0.2	1793.7	31.7	38.0	0.4	1806.2	29.0	22.2	0.7
	0.3	1802.7	40.5	36.6	0.1	1556.4	41.2	20.1	0.3

Table A.2
Mechanical properties of specimens with a longitudinal and transverse raster orientations at a strain rate of $3 \cdot 10^{-3} s^{-1}$.

Specimen		Longitudinal				Transverse			
Number of layers	Layer	Elastic modulus (MPa)		Maximum stress (MPa)		Elastic modulus (MPa)		Maximum stress (MPa)	
	Height (mm)	Mean	SD	Mean	SD	Mean	SD	Mean	SD
1	0.1	2317.6	54.7	48.9	0.6	2017.8	19.4	23.0	0.9
	0.2	2063.2	14.0	43.3	0.3	1916.4	40.3	16.4	1.3
	0.3	2012.2	21.3	40.8	0.4	1629.9	15.8	22.8	0.1
2	0.1	2098.0	39.0	45.2	0.6	2039.1	56.4	21.2	5.5
	0.2	1971.6	26.0	42.3	0.4	1865.3	56.4	20.4	1.2
	0.3	1918.3	44.6	41.1	0.3	1645.8	60.4	20.1	2.0
3	0.1	1880.9	97.6	45.6	0.5	1983.8	39.6	28.4	2.2
	0.2	1921.8	13.8	41.9	0.2	1872.5	38.3	22.9	0.8
	0.3	1922.7	65.8	39.4	0.7	1621.1	22.1	23.5	0.6

provides a continuum model to predict the final macroscopic mechanical response of FDM components. This model, along with previous modelling approaches to describe the FDM process [21], postulates as a relevant tool to aid at the design of customised FDM structures. However, it is worth to mention that the model has been tested and validated against uniaxial loading. Therefore, although the present work provides a significant advance in the constitutive modelling of 3D printed polymers, further efforts are needed to provide a complete formulation to describe accurately the response of such materials within a wider range of loading conditions.

CRediT authorship contribution statement

S. Garzon-Hernandez: Investigation, Methodology, Formal analysis, Writing - original draft, Writing review & editing. **A. Arias:** Investigation, Formal analysis, Writing - review & editing. **D. Garcia-Gonzalez:** Investigation, Methodology, Formal analysis, Writing - review & editing.

Declaration of competing interest

The authors declare that they have no known competing financial interests or personal relationships that could have appeared to influence the work reported in this paper.

Acknowledgements

The authors acknowledge support from Ministerio de Ciencia, Innovación y Universidades, Spain, Agencia Estatal de Investigación y Fondo Europeo de Desarrollo Regional, Spain, como entidades financiadoras (RTI2018-094318-B-I00). D.G.-G., S.G.-H. and A.A. acknowledge support from Programa de Apoyo a la Realización de Proyectos Interdisciplinares de I+D para Jóvenes Investigadores de la Universidad Carlos III de Madrid (BIOMASKIN-CM-UC3M). D.G.-G. acknowledges support from the Talent Attraction grant (CM 2018 - 2018-T2/IND-9992) from the Comunidad de Madrid, Spain.

Appendix

The results in terms of Young's modulus and maximum stress are shown in Tables A.1 and A.2. The maximum stress corresponds to the yield stress for longitudinal specimens and to the ultimate tensile strength for transverse specimens.

The values of standard deviation show good repeatability in the results. However, some scatter is observed in the maximum stress for transverse specimens. These values correspond with the ultimate tensile strength, which is highly influenced by the defects of the components.

References

[1] Srivatsan T, Sudarshan T. Additive Manufacturing: Innovations, Advances, and Applications. CRC Press; 2015.

[2] Ngo TD, Kashani A, Imbalzano G, Nguyen KT, Hui D. Additive manufacturing (3D printing): A review of materials, methods, applications and challenges. Composites B 2018;143:172–96. http://dx.doi.org/10.1016/j.compositesb.2018.02.012, http://www.sciencedirect.com/science/article/pii/S1359836817342944.

[3] Domingo-Espin M, Puigoriol-Forcada JM, Garcia-Granada A-A, Llumà J, Borros S, Reyes G. Mechanical property characterization and simulation of fused deposition modeling polycarbonate parts. Mater Des 2015;83:670–7. http://dx.doi.org/10.1016/j.matdes.2015.06.074, http://www.sciencedirect.com/science/article/pii/S0264127515004244.

[4] Zaldivar R, Witkin D, McLouth T, Patel D, Schmitt K, Nokes J. Influence of processing and orientation print effects on the mechanical and thermal behavior of 3D-printed ultem 9085 material. Addit Manuf 2017;13:71–80. http://dx.doi.org/10.1016/j.addma.2016.11.007, http://www.sciencedirect.com/science/article/pii/S2214860416301609.

[5] Ding S, Zou B, Wang P, Ding H. Effects of nozzle temperature and building orientation on mechanical properties and microstructure of PEEK and PEI printed by 3D-FDM. Polym Test 2019;78:105948. http://dx.doi.org/10.1016/j.polymertesting.2019.105948, http://www.sciencedirect.com/science/article/pii/S0142941819304994.

[6] Heidari-Rarani M, Rafiee-Afarani M, Zahedi A. Mechanical characterization of FDM 3D printing of continuous carbon fiber reinforced PLA composites. Composites B 2019;175:107147. http://dx.doi.org/10.1016/j.compositesb.2019.107147, http://www.sciencedirect.com/science/article/pii/S1359836818335686.

[7] Chacón J, Caminero M, Núez P, a Plaza EG, a Moreno IG, Reverte J. Additive manufacturing of continuous fibre reinforced thermoplastic composites using fused deposition modelling: Effect of process parameters on mechanical properties. Compos Sci Technol 2019;181:107688. http://dx.doi.org/10.1016/j.compscitech.2019.107688, http://www.sciencedirect.com/science/article/pii/S0266353818313162.

[8] Wang X, Jiang M, Zhou Z, Gou J, Hui D. 3D Printing of polymer matrix composites: A review and prospective. Composites B 2017;110:442–58. http://dx.doi.org/10.1016/j.compositesb.2016.11.034, http://www.sciencedirect.com/science/article/pii/S1359836816321230.

[9] Rodríguez JF, Thomas JP, Renaud JE. Mechanical behavior of acrylonitrile butadiene styrene (ABS) fused deposition materials. experimental investigation. Rapid Prototyping J 2001;7(3):148–58. http://dx.doi.org/10.1108/13552540110395547.

[10] Vairis A, Petousis M, Vidakis N, Savvakis K. On the strain rate sensitivity of abs and abs plus fused deposition modeling parts. J Mater Eng Perform 2016;25(9):3558–65. http://dx.doi.org/10.1007/s11665-016-2198-x, https://doi.org/10.1007/s11665-016-2198-x.

[11] Song Y, Li Y, Song W, Yee K, Lee K-Y, Tagarielli V. Measurements of the mechanical response of unidirectional 3D-printed PLA. Mater Des 2017;123:154–64. http://dx.doi.org/10.1016/j.matdes.2017.03.051, http://www.sciencedirect.com/science/article/pii/S0264127517302976.

[12] Sood AK, Ohdar R, Mahapatra S. Parametric appraisal of mechanical property of fused deposition modelling processed parts. Mater Des 2010;31(1):287–95. http://dx.doi.org/10.1016/j.matdes.2009.06.016, http://www.sciencedirect.com/science/article/pii/S0261306909002945.

[13] Rankouhi B, Javadpour S, Delfanian F, Letcher T. Failure analysis and mechanical characterization of 3D printed ABS with respect to layer thickness and orientation. J Failure Anal Prevent 2016;16(3):467–81. http://dx.doi.org/10.1007/s11668-016-0113-2, https://doi.org/10.1007/s11668-016-0113-2.

[14] Wang P, Zou B, Xiao H, Ding S, Huang C. Effects of printing parameters of fused deposition modeling on mechanical properties, surface quality, and microstructure of PEEK. J Mater Process Technol 2019;271:62–74. http://dx.doi.org/10.1016/j.jmatprotec.2019.03.016, http://www.sciencedirect.com/science/article/pii/S0924013619301049.

[15] Ahn S, Montero M, Odell D, Roundy S, Wright PK. Anisotropic material properties of fused deposition modeling ABS. Rapid Prototyping J 2002;8(4):248–57. http://dx.doi.org/10.1108/13552540210441166.

[16] Aliheidari N, Tripuraneni R, Ameli A, Nadimpalli S. Fracture resistance measurement of fused deposition modeling 3D printed polymers. Polym Test 2017;60:94–101. http://dx.doi.org/10.1016/j.polymertesting.2017.03.016, http://www.sciencedirect.com/science/article/pii/S0142941817300065.

[17] Chacón J, Caminero M, a Plaza EG, Núez P. Additive manufacturing of PLA structures using fused deposition modelling: Effect of process parameters on mechanical properties and their optimal selection. Mater Des 2017;124:143–57. http://dx.doi.org/10.1016/j.matdes.2017.03.065, http://www.sciencedirect.com/science/article/pii/S0264127517303143.

[18] Ziemian C, Sharma M, Ziemian S. Anisotropic mechanical properties of ABS parts fabricated by fused deposition modelling. In: Gokcek M, editor. Mechanical Engineering. Rijeka: IntechOpen; 2012, http://dx.doi.org/10.5772/34233, https://doi.org/10.5772/34233.

[19] Torrado AR, Roberson DA. Failure analysis and anisotropy evaluation of 3D-printed tensile test specimens of different geometries and print raster patterns. J Failure Anal Prevent 2016;16(1):154–64. http://dx.doi.org/10.1007/s11668-016-0067-4, https://doi.org/10.1007/s11668-016-0067-4.

[20] Zou R, Xia Y, Liu S, Hu P, Hou W, Hu Q, Shan C. Isotropic and anisotropic elasticity and yielding of 3D printed material. Composites B 2016;99:506–13. http://dx.doi.org/10.1016/j.compositesb.2016.06.009, http://www.sciencedirect.com/science/article/pii/S1359836816309052.

[21] Garzon-Hernandez S, Garcia-Gonzalez D, Jérusalem A, Arias A. Design of FDM 3D printed polymers: An experimental-modelling methodology for the prediction of mechanical properties. Mater Design 2020;188:108414. http://dx.doi.org/10.1016/j.matdes.2019.108414, http://www.sciencedirect.com/science/article/pii/S0264127519308524.

[22] Arruda EM, Boyce MC. Evolution of plastic anisotropy in amorphous polymers during finite straining. Int J Plast 1993;9(6):697–720. http://dx.doi.org/10.1016/0749-6419(93)90034-N, http://www.sciencedirect.com/science/article/pii/074964199390034N.

[23] Mulliken A, Boyce M. Mechanics of the rate-dependent elastic–plastic deformation of glassy polymers from low to high strain rates. Int J Solids Struct 2006;43(5):1331–56. http://dx.doi.org/10.1016/j.ijsolstr.2005.04.016, http://www.sciencedirect.com/science/article/pii/S0020768305002313.

[24] Polanco-Loria M, Clausen AH, Berstad T, Hopperstad OS. Constitutive model for thermoplastics with structural applications. Int J Impact Eng 2010;37(12):1207–19. http://dx.doi.org/10.1016/j.ijimpeng.2010.06.006, http://www.sciencedirect.com/science/article/pii/S0734743X10001065.

[25] Ognedal AS, Clausen AH, Polanco-Loria M, Benallal A, Raka B, Hopperstad OS. Experimental and numerical study on the behaviour of PVC and HDPE in biaxial tension. Mech Mater 2012;54:18–31. http://dx.doi.org/10.1016/j.mechmat.2012.05.010, http://www.sciencedirect.com/science/article/pii/S0167663612001123.

[26] Nguyen V-D, Lani F, Pardoen T, Morelle X, Noels L. A large strain hyperelastic viscoelastic-viscoplastic-damage constitutive model based on a multi-mechanism non-local damage continuum for amorphous glassy polymers. Int J Solids Struct 2016;96:192–216. http://dx.doi.org/10.1016/j.ijsolstr.2016.06.008, http://www.sciencedirect.com/science/article/pii/S0020768316301238.

[27] Garcia-Gonzalez D, Zaera R, Arias A. A hyperelastic-thermoviscoplastic constitutive model for semi-crystalline polymers: Application to PEEK under dynamic loading conditions. Int J Plast 2017;88:27–52. http://dx.doi.org/10.1016/j.ijplas.2016.09.011, http://www.sciencedirect.com/science/article/pii/S0749641916301760.

[28] Garcia-Gonzalez D, Garzon-Hernandez S, Arias A. A new constitutive model for polymeric matrices: Application to biomedical materials. Composites B 2018;139:117–29. http://dx.doi.org/10.1016/j.compositesb.2017.11.045, http://www.sciencedirect.com/science/article/pii/S1359836817324496.

[29] Barba D, Arias A, Garcia-Gonzalez D. Temperature and strain rate dependences on hardening and softening behaviours in semi-crystalline polymers: Application to PEEK. Int J Solids Struct 2020. http://dx.doi.org/10.1016/j.ijsolstr.2019.08.021, http://www.sciencedirect.com/science/article/pii/S0020768319303890.

[30] Sumelka W. Fractional viscoplasticity. Mech Res Commun 2014;56:31–6. http://dx.doi.org/10.1016/j.mechrescom.2013.11.005, http://www.sciencedirect.com/science/article/pii/S0093641313001961.

[31] Voyiadjis GZ, Sumelka W. Brain modelling in the framework of anisotropic hyperelasticity with time fractional damage evolution governed by the caputo-almeida fractional derivative. J Mech Behav Biomed Mater 2019;89:209–16. http://dx.doi.org/10.1016/j.jmbbm.2018.09.029, http://www.sciencedirect.com/science/article/pii/S1751616118310336.

[32] Alaimo G, Marconi S, Costato L, Auricchio F. Influence of meso-structure and chemical composition on FDM 3D-printed parts. Composites B 2017;113:371–80. http://dx.doi.org/10.1016/j.compositesb.2017.01.019, http://www.sciencedirect.com/science/article/pii/S1359836816330037.

[33] Somireddy M, Czekanski A, Singh CV. Development of constitutive material model of 3D printed structure via FDM. Mater Today Commun 2018;15:143–52. http://dx.doi.org/10.1016/j.mtcomm.2018.03.004, http://www.sciencedirect.com/science/article/pii/S2352492818300552.

[34] Letcher T, Rankouhi B, Javadpour S. Experimental study of mechanical properties of additively manufactured ABS plastic as a function of layer parameters. 2015, http://dx.doi.org/10.1115/IMECE2015-52634.

[35] Croccolo D, Agostinis MD, Olmi G. Experimental characterization and analytical modelling of the mechanical behaviour of fused deposition processed parts made of ABS-M30. Comput Mater Sci 2013;79:506–18. http://dx.doi.org/10.1016/j.commatsci.2013.06.041, http://www.sciencedirect.com/science/article/pii/S0927025613003741.

[36] Greenhalgh ES. 4 - Delamination-dominated failures in polymer composites. In: Greenhalgh ES, editor. Failure Analysis and Fractography of Polymer Composites. Woodhead Publishing Series in Composites Science and Engineering, Woodhead Publishing; 2009, p. 164–237. http://dx.doi.org/10.1533/9781845696818.164, http://www.sciencedirect.com/science/article/pii/B9781845692179500044.

[37] Coleman BD, Noll W. The thermodynamics of elastic materials with heat conduction and viscosity. Arch Ration Mech Anal 1963;13(1):167–78. http://dx.doi.org/10.1007/BF01262690, https://doi.org/10.1007/BF01262690.

[38] Coleman BDD, Gurtin ME. Thermodynamics with internal state variables. 1967, http://dx.doi.org/10.1184/R1/6480089.v1, https://kilthub.cmu.edu/articles/Thermodynamics_with_internal_state_variables/6480089.

[39] Bellehumeur C, Li L, Sun Q, Gu P. Modeling of bond formation between polymer filaments in the fused deposition modeling process. J Manuf Process 2004;6(2):170–8. http://dx.doi.org/10.1016/S1526-6125(04)70071-7, http://www.sciencedirect.com/science/article/pii/S1526612504700717.

[40] Guo Z, Caner F, Peng X, Moran B. On constitutive modelling of porous neo-hookean composites. J Mech Phys Solids 2008;56(6):2338–57. http://dx.doi.org/10.1016/j.jmps.2007.12.007, http://www.sciencedirect.com/science/article/pii/S0022509607002554.

[41] Kachanov M, Tsukrov I, Shafiro B. Effective moduli of solids with cavities of various shapes. Appl Mech Rev 1994;47. http://dx.doi.org/10.1115/1.3122810.

[42] Kováčik J. Correlation between shear modulus and porosity in porous materials. J Mater Sci Lett 2001;20(21):1953–5. http://dx.doi.org/10.1023/A:1013186702962, https://doi.org/10.1023/A:1013186702962.

[43] Garcia-Gonzalez D. Magneto-visco-hyperelasticity for hard-magnetic soft materials: theory and numerical applications. Smart Mater Struct 2019;28(8):085020. http://dx.doi.org/10.1088/1361-665x/ab2b05.

[44] Garcia-Gonzalez D, Landis C. Magneto-diffusion-viscohyperelasticity for magneto-active hydrogels: rate dependences across time scales. J. Mech. Phys. Solids 2020;139:103934. http://dx.doi.org/10.1016/j.jmps.2020.103934.

[45] Samadi-Dooki A, Malekmotiei L, Voyiadjis GZ. Characterizing shear transformation zones in polycarbonate using nanoindentation. Polymer 2016;82:238–45. http://dx.doi.org/10.1016/j.polymer.2015.11.049, http://www.sciencedirect.com/science/article/pii/S0032386115304067.

[46] Voyiadjis G, Samadi-Dooki A. Constitutive modeling of large inelastic deformation of amorphous polymers: Free volume and shear transformation zone dynamics. J Appl Phys 2016;119:225104. http://dx.doi.org/10.1063/1.4953355.

[47] Jeridi M, Laiarinandrasana L, Sa K. Comparative study of continuum damage mechanics and mechanics of porous media based on multi-mechanism model on polyamide 6 semi-crystalline polymer. Int J Solids Struct 2015;53:12–27. http://dx.doi.org/10.1016/j.ijsolstr.2014.10.031, http://www.sciencedirect.com/science/article/pii/S0020768314004107.

[48] Oral A, Anlas G, Lambros J. Determination of gurson–tvergaard–needleman model parameters for failure of a polymeric material. Int J Damage Mech 2012;21:3–25. http://dx.doi.org/10.1177/1056789510385261.

[49] Gurson A. Continuum theory of ductile rupture by void nucleation and growth: Part I—Yield criteria and flow rules for porous ductile media. Trans ASME 1977;99. http://dx.doi.org/10.1115/1.3443401.

[50] Tvergaard V. Influence of voids on shear band instabilities under plane strain conditions. Int J Fract 1981;17(4):389–407. http://dx.doi.org/10.1007/BF00036191, https://doi.org/10.1007/BF00036191.

[51] Tvergaard V. Effect of yield surface curvature and void nucleation on plastic flow localization. J Mech Phys Solids 1987;35(1):43–60. http://dx.doi.org/10.1016/0022-5096(87)90027-5, http://www.sciencedirect.com/science/article/pii/0022509687900275.

[52] Boyce M, Socrate S, Llana P. Constitutive model for the finite deformation stress–strain behavior of poly(ethylene terephthalate) above the glass transition. Polymer 2000;41(6):2183–201. http://dx.doi.org/10.1016/S0032-3861(99)00406-1, http://www.sciencedirect.com/science/article/pii/S0032386199004061.

[53] Garcia-Gonzalez D, Jérusalem A, Garzon-Hernandez S, Zaera R, Arias A. A continuum mechanics constitutive framework for transverse isotropic soft tissues. J Mech Phys Solids 2018;112:209–24. http://dx.doi.org/10.1016/j.jmps.2017.12.001, http://www.sciencedirect.com/science/article/pii/S0022509617304921.